The Astrophysical Journal Letters, 994:L9 (15pp), 2025 November 20 https://doi.org/10.3847/2041-8213/ae157d

Detection of Compton Scattering in the Jet of 3C 84

Ioannis Liodakis[1,2], Sudip Chakraborty[3], Frédéric Marin[4], Steven R. Ehlert[3], Thibault Barnouin[4], Pouya M. Kouch[5,6], Kari Nilsson[5], Elina Lindfors[7], Tapio Pursimo[8,9], Georgios F. Paraschos[2], Riccardo Middei[10,11,12], Anna Trindade Falcão[13,14], Svetlana Jorstad[15,16], Iván Agudo[17], Yuri Y. Kovalev[2], Jacob J. Casey[18], Laura Di Gesu[19], Philip Kaaret[3], Dawoon E. Kim[20], Fabian Kislat[18], Ajay Ratheesh[20,21], M. Lynne Saade[3,22], Francesco Tombesi[23,24], Alan Marscher[15], Francisco José Aceituno[25], Giacomo Bonnoli[25,26], Víctor Casanova[25], Gabriel Emery[25], Juan Escudero Pedrosa[12,17], Daniel Morcuende[25], Jorge Otero-Santos[17,27], Alfredo Sota[25], Vilppu Piirola[6], Rumen Bachev[28], Anton Strigachev[28], George A. Borman[29], Tatiana S. Grishina[16], Vladimir A. Hagen-Thorn[16], Evgenia N. Kopatskaya[16], Elena G. Larionova[16], Daria A. Morozova[16], Sergey S. Savchenko[16,30], Ekaterina V. Shishkina[16], Ivan S. Troitskiy[16], Yulia V. Troitskaya[16], Andrey A. Vasilyev[16], Alexey V. Zhovtan[29], Ioannis Myserlis[31], Mark Gurwell[12], Garrett Keating[12], Ramprasad Rao[12], Sincheol Kang[32], Sang-Sung Lee[32,33], Sanghyun Kim[32], Whee Yeon Cheong[32], Hyeon-Woo Jeong[32,33], Chanwoo Song[32,33], Shan Li[32,33], Myeong-Seok Nam[32,33], Diego Álvarez-Ortega[1,34], Carolina Casadio[1,34], Emmanouil Angelakis[35], Alexander Kraus[2], Jenni Jormanainen[5,7], Vandad Fallah Ramazani[5,36], Chien-Ting Chen[37], Enrico Costa[38], Eugene Churazov[39], Riccardo Ferrazzoli[38], Giorgio Galanti[40], Ildar Khabibullin[39,41], Stephen L. O'Dell[3], Luigi Pacciani[42], Marco Roncadelli[43], Oliver J. Roberts[37], Paolo Soffitta[38], Douglas A. Swartz[37], Fabrizio Tavecchio[26], Martin C. Weisskopf[3], and Irina Zhuravleva[44]

[1] Institute of Astrophysics, Foundation for Research and Technology—Hellas, Voutes, 70013 Heraklion, Greece; liodakis@ia.forth.gr
[2] Max-Planck-Institut für Radioastronomie, Auf dem Hügel 69, D-53121 Bonn, Germany
[3] NASA Marshall Space Flight Center, Huntsville, AL 35812, USA
[4] Université de Strasbourg, CNRS, Observatoire Astronomique de Strasbourg, UMR 7550, 67000 Strasbourg, France
[5] Finnish Centre for Astronomy with ESO (FINCA), 20014 University of Turku, Finland
[6] Department of Physics and Astronomy, 20014 University of Turku, Finland
[7] Department of Physics and Astronomy, Quantum, Vesilinnantie 5, FI-20014 University of Turku, Finland
[8] Nordic Optical Telescope, Apartado 474, E-38700 Santa Cruz de La Palma, Santa Cruz de Tenerife, Spain
[9] Department of Physics and Astronomy, Aarhus University, Munkegade 120, DK-8000 Aarhus C, Denmark
[10] Space Science Data Center, Agenzia Spaziale Italiana, Via del Politecnico snc, I-00133 Roma, Italy
[11] INAF Osservatorio Astronomico di Roma, Via Frascati 33, 00078 Monte Porzio Catone (RM), Italy
[12] Center for Astrophysics | Harvard & Smithsonian, 60 Garden Street, Cambridge, MA 02138, USA
[13] Harvard-Smithsonian Center for Astrophysics, 60 Garden Street, Cambridge, MA 02138, USA
[14] NASA-Goddard Space Flight Center, Code 662, Greenbelt, MD 20771, USA
[15] Institute for Astrophysical Research, Boston University, 725 Commonwealth Avenue, Boston, MA 02215, USA
[16] Saint Petersburg State University, 7/9 Universitetskaya nab., St. Petersburg, 199034, Russia
[17] Instituto de Astrofísica de Andalucía, IAA-CSIC, Glorieta de la Astronomía s/n, E-18008 Granada, Spain
[18] Department of Physics and Astronomy and Space Science Center, University of New Hampshire, Durham, NH 03824, USA
[19] ASI—Agenzia Spaziale Italiana, Via del Politecnico snc, 00133 Roma, Italy
[20] INAF, Istituto di Astrofisica e Planetologia Spaziali, Via Fosso del Cavaliere 100, 00133 Roma, Italy
[21] Physical Research Laboratory, Thaltej, Ahmedabad, Gujarat 380009, India
[22] Science & Technology Institute, Universities Space Research Association, 320 Sparkman Drive, Huntsville, AL 35805, USA
[23] Dipartimento di Fisica, Universitá degli Studi di Roma "Tor Vergata," Via della Ricerca Scientifica 1, 00133 Roma, Italy
[24] Istituto Nazionale di Fisica Nucleare, Sezione di Roma "Tor Vergata," Via della Ricerca Scientifica 1, 00133 Roma, Italy
[25] Instituto de Astrofísica de Andalucía, IAA-CSIC, Glorieta de la Astronomía s/n, 18008 Granada, Spain
[26] INAF Osservatorio Astronomico di Brera, Via E. Bianchi 46, 23807 Merate (LC), Italy
[27] Istituto Nazionale di Fisica Nucleare, Sezione di Padova, 35131 Padova, Italy
[28] Institute of Astronomy and NAO, Bulgarian Academy of Sciences, 1784 Sofia, Bulgaria
[29] Crimean Astrophysical Observatory RAS, P/O Nauchny, 298409, Crimea†
[30] Pulkovo Observatory, St. Petersburg, 196140, Russia
[31] Institut de Radioastronomie Millimétrique, Avenida Divina Pastora, 7, Local 20, E-18012 Granada, Spain
[32] Korea Astronomy and Space Science Institute, 776 Daedeok-daero, Yuseong-gu, Daejeon 34055, Republic of Korea
[33] University of Science and Technology, Korea, 217 Gajeong-ro, Yuseong-gu, Daejeon 34113, Republic of Korea
[34] Department of Physics, University of Crete, 70013, Heraklion, Greece
[35] Section of Astrophysics, Astronomy & Mechanics, Department of Physics, National and Kapodistrian University of Athens, Panepistimiopolis Zografos 15784, Greece
[36] Aalto University Metsähovi Radio Observatory, Metsähovintie 114, FI-02540 Kylmälä, Finland
[37] Science and Technology Institute, Universities Space Research Association, Huntsville, AL 35805, USA
[38] INAF Istituto di Astrofisica e Planetologia Spaziali, Via del Fosso del Cavaliere 100, 00133 Roma, Italy
[39] Max Planck Institute for Astrophysics, Karl-Schwarzschild-Str. 1, D-85741 Garching, Germany
[40] INAF, Istituto di Astrofisica Spaziale e Fisica Cosmica di Milano, Via Alfonso Corti 12, I-20133 Milano, Italy
[41] Universitäts-Sternwarte, Fakultät fuer Physik, Ludwig-Maximilians-Universität Muenchen, Scheinerstr.1, 81679 Muenchen, Germany
[42] INAF, Istituto di Astrofisica e Planetologia Spaziali, Via Fosso del Cavaliere, 100—I-00133 Rome, Italy
[43] INFN, Sezione di Pavia, Via A. Bassi 6, 27100 Pavia, Italy

[44] Department of Astronomy and Astrophysics, The University of Chicago, Chicago, IL 60637, USA
Received 2025 August 27; revised 2025 October 13; accepted 2025 October 17; published 2025 November 11

Abstract

3C 84 is the brightest cluster galaxy in the Perseus Cluster. It is among the closest radio-loud active galaxies and among the very few that can be detected from low-frequency radio up to TeV γ-rays. Here we report on the first X-ray polarization observation of 3C 84 with the Imaging X-ray Polarimetry Explorer, for a total of 2.2 Ms coinciding with a flare in γ-rays. This is the longest observation for a radio-loud active galaxy, which allowed us to reach unprecedented sensitivity, leading to the detection of an X-ray polarization degree of $\Pi_X = 4.2\% \pm 1.3\%$ ($\sim 3.2\sigma$ confidence) at an X-ray electric vector polarization angle of $\psi_X = 163^\circ \pm 9^\circ$, which is aligned with the radio jet direction on the sky. Optical polarization observations show fast variability about the jet axis as well. Our results strongly favor models in which X-rays are produced by Compton scattering from relativistic electrons—specifically synchrotron self-Compton—that takes place downstream, away from the supermassive black hole.

Unified Astronomy Thesaurus concepts: Black hole physics (159); Radio active galactic nuclei (2134); Jets (870); Polarimetry (1278); Perseus Cluster (1214); Brightest cluster galaxies (181); Relativistic jets (1390)

1. Introduction

3C 84 (also known as NGC 1275) is among the nearest and brightest radio galaxies, located in the Perseus Cluster. It is an FR I, Seyfert 2–type galaxy (E. Y. Khachikian & D. W. Weedman 1974) that would be equivalent to a BL Lacertae–type object according to the active galactic nuclei (AGN) unification scheme (R. Antonucci 1993). At radio wavelengths it shows a spine-sheath morphology (e.g., H. Nagai et al. 2014; G. Giovannini et al. 2018; G. F. Paraschos et al. 2024a) with a magnetic field of a few gauss at parsec scales (J. Y. Kim et al. 2019; G. F. Paraschos et al. 2021, 2023) potentially driving Kelvin–Helmoltz instabilities (G. F. Paraschos & V. Mpisketzis 2025). Recent Event Horizon Telescope observations at 228 GHz showed regions with highly ordered magnetic fields reaching a polarization degree of $\sim$17% (G. F. Paraschos et al. 2024b).

Despite showing a low jet speed and Doppler factor (e.g., I. Liodakis et al. 2018a; G. F. Paraschos et al. 2022; Z. R. Weaver et al. 2022), its multiwavelength behavior is quite intriguing. Unlike other radio galaxies, 3C 84 has variable high-energy emission (e.g., Y. Fukazawa et al. 2018; B. Rani et al. 2018; F. Imazato et al. 2021), shows bright γ-ray behavior at GeV energies (A. A. Abdo et al. 2009), and has even been detected in TeV γ-rays (J. Aleksić et al. 2014; Z. Cao et al. 2024). The origin of the high-energy emission in radio galaxies in general and in 3C 84 in particular is still a matter of debate. If the emission is dominated by the jet, it will originate either from relativistic electrons upscattering low-energy photons to X-rays and γ-rays (e.g., J. Poutanen 1994; A. Mastichiadis & J. G. Kirk 1997; M. Böttcher et al. 2013) or from proton processes that include proton synchrotron and pair cascades from secondary particles created in proton–photon interactions (e.g., K. Mannheim 1993; A. Mastichiadis 1996; H. Zhang & M. Böttcher 2013; A. Mastichiadis & M. Petropoulou 2021). On the other hand, if the emission is dominated by the accretion disk, the high-energy emission will be dominated by the hot corona (e.g., F. Haardt & L. Maraschi 1991; E. Kara et al. 2016). Depending on the inclination of the source, the emission will be either direct corona emission or reflection from Compton-thick material surrounding the accretion disk (e.g., V. Singh et al. 2011). Recent X-ray observations from the Imaging X-ray Polarimetry Explorer (IXPE; M. C. Weisskopf et al. 2022; P. Soffitta et al. 2023) have confirmed this picture (V. E. Gianolli et al. 2023; A. Ingram et al. 2023; D. Tagliacozzo et al. 2023; F. Ursini et al. 2023; F. Marin et al. 2024; S. Chakraborty et al. 2025).

Previous studies on 3C 84 suggest that the X-ray emission is dominated by the jet (B. Rani et al. 2018), while γ-rays could originate from multiple emission sites (J. A. Hodgson et al. 2018, 2021; G. F. Paraschos et al. 2023; V. G. Sinitsyna & V. Y. Sinitsyna 2025). The high-energy emission is thought to originate from synchrotron self-Compton from relativistic electrons (e.g., J. Aleksić et al. 2014; K. Tanada et al. 2018; Z. Cao et al. 2024) that are likely accelerated in shocks (Y. Fukazawa et al. 2018). IXPE observations of low-synchrotron (S. R. Ehlert et al. 2022; H. L. Marshall et al. 2024; R. Middei et al. 2023a; I. Agudo et al. 2025; P. M. Kouch et al. 2025) and high-synchrotron peak blazars (I. Liodakis et al. 2022; L. Di Gesu et al. 2023; S. R. Ehlert et al. 2023; R. Middei et al. 2023b; C.-T. J. Chen et al. 2024; P. M. Kouch et al. 2024; S. Capecchiacci et al. 2025) are also consistent with such scenarios.

Apart from 3C 84 discussed here, IXPE has observed two more radio galaxies: Centaurus A (S. R. Ehlert et al. 2022), which showed low X-ray polarization ($<$8% at 99% confidence), and Pictor A, focusing on the western hot spot (S. Tugliani et al. 2025). Here we report on the first X-ray polarization observation of 3C 84, aiming to understand the origin of its X-ray emission. In Section 2 we describe the novel X-ray polarization observations and the multiwavelength campaign that accompanied them, and in Section 3 we discuss our findings and present our conclusions. Additional details on our analysis are given in Appendices A and B.

2. Multiwavelength Polarization Observations

2.1. X-Ray Polarization Observations

The IXPE observations of 3C 84 were taken in five separate segments between 2025 January 26 and 2025 March 26. The total exposure before filtering for flares is 2.19 Ms (Figure 1). We perform good time interval (GTI) filtering of the light curve in the 8–10 keV band (where the mirrors have no effective area) to identify time intervals where solar flares may

[†] While the AAS journals adhere to and respect UN resolutions regarding the designations of territories (available at http://www.un.org/press/en), it is our policy to use the affiliations provided by our authors on published articles.

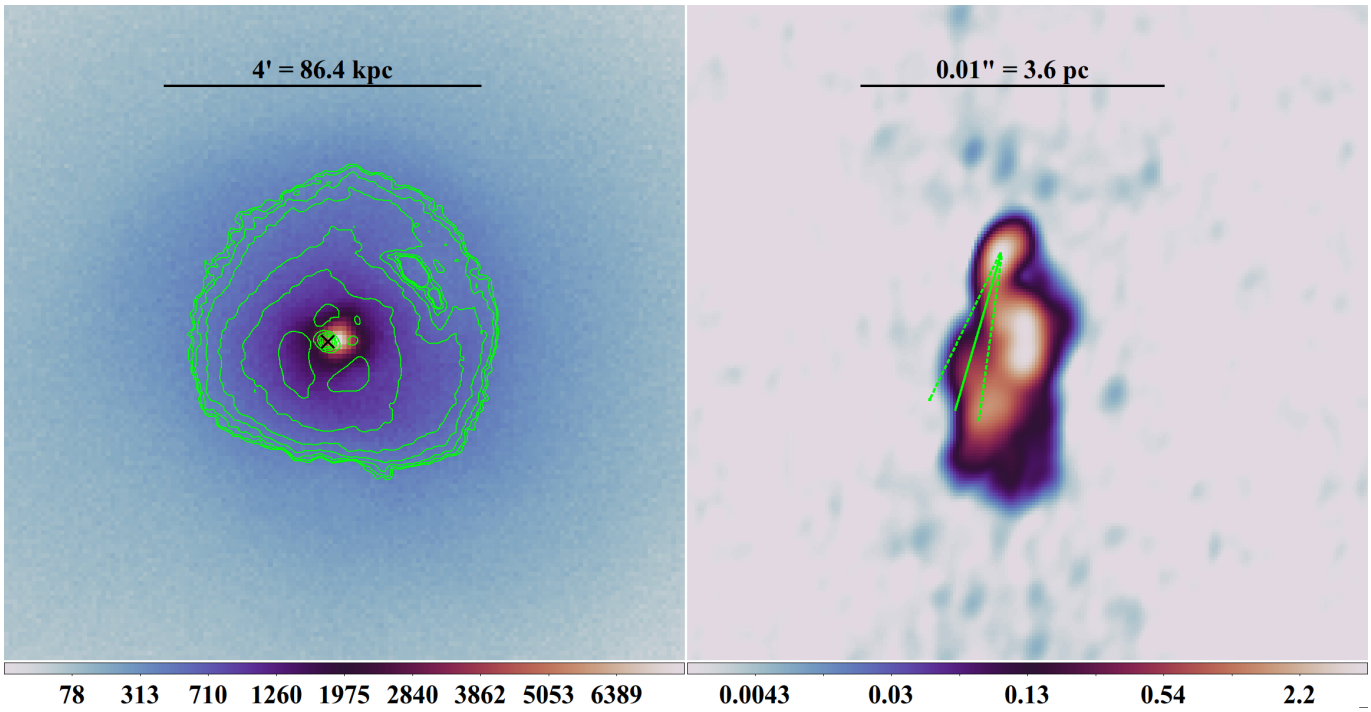

Figure 1. Left: IXPE counts image of the Perseus Cluster overlaid with surface brightness contours from Chandra, showing that many of the substructures clearly apparent in the higher angular resolution Chandra data are also visible at lower resolution in IXPE. The black cross corresponds to the position of 3C 84. Right: cleaned 15 GHz Stokes*I*VLBA image of the parsec-scale jet of 3C 84, observed as part of the MOJAVE program on 2025 February 21, in units of Jy beam^{-1}. Notice that the angular scale of this radio image is approximately three orders of magnitude smaller than the IXPE image. Overlaid in green is the X-ray polarization vector with the 1σ confidence interval of the polarization angle denoted by the two dashed lines. The polarization vector's direction is fully consistent with the direction of the radio jet.

dominate the astrophysical X-ray signal. We also exclude 59 ks (see Appendix A.1 for more details). A small enhancement in the IXPE count rate is observed during this time period, and although the duration and intensity of the flare correspond to only a small perturbation to the integrated signal, we conservatively exclude this time period out of an abundance of caution. After all filtering, the total exposure time is 2.13 Ms. For all subsequent results, all events identified as background using the algorithm of A. Di Marco et al. (2023) have been filtered out a priori. All results presented, unless otherwise noted, are for the entire 2–8 keV IXPE bandpass.

Time-resolved spectroscopy of the IXPE data within a $1'$-radius aperture centered on 3C 84 during the cleaned GTIs shows no evidence of additional variability in the overall flux or power-law photon index with time. As measured by IXPE, the overall flux of 3C 84 in this aperture is $\sim 1.5 \times 10^{-11}$ erg cm^{-2} s^{-1} and $\Gamma \sim 1.8$.

We measure the polarization of 3C 84 by performing a spectropolarimetric fit to the IXPE data in the 2–8 keV band alongside Chandra, Swift X-Ray Telescope (XRT), and NuSTAR observations of the Perseus Cluster. This joint fit is required to separate the polarized power-law emission from the expected thermal emission from the intracluster medium (ICM), and the details for how the spectra are extracted and modeled can be found in Appendix A.2. For the IXPE data, we use a source aperture of $30''$ in radius (see Appendix A.2.1 for details and justification). From this fit, we find a polarization degree of $\Pi_X = 4.18\% \pm 1.31\%$ and an angle of $\psi_X = 162.^\circ 8 \pm 9.^\circ 2$, consistent with the simpler model-independent value. The corresponding 2–8 keV minimum detectable polarization at 99% (MDP$_{99}$), excluding the diffused background, is 2.39%. The polarization contours for this model fit are shown in Figure 2. Extensive testing and analysis using data from Chandra, NuSTAR, and Swift alongside the extracted IXPE Stokes $I/Q/U$ spectra have shown that the significance of the detection is robust to a large range of assumptions regarding the thermal emission of the Perseus Cluster and the non-X-ray background (NXB) in the IXPE data. An image of the Perseus Cluster as observed by IXPE, as well as the X-ray polarization vector superimposed on the Very Long Baseline Array (VLBA; MOJAVE) observations, can be found in Figure 1.

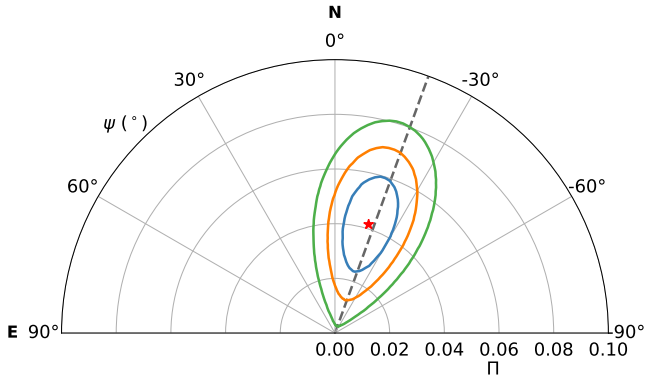

Figure 2. Polarization contours for 3C 84 using a spectropolarimetric model fit. The red star denotes the best-fit value, while the blue, orange, and green contours correspond to 1σ, 2σ, and 3σ confidence intervals. The dashed line corresponds to the position angle of the radio jet.

2.2. Radio and Optical Polarization Observations

Contemporaneous to the IXPE observation, we initiated a multiwavelength campaign that included several ground-based

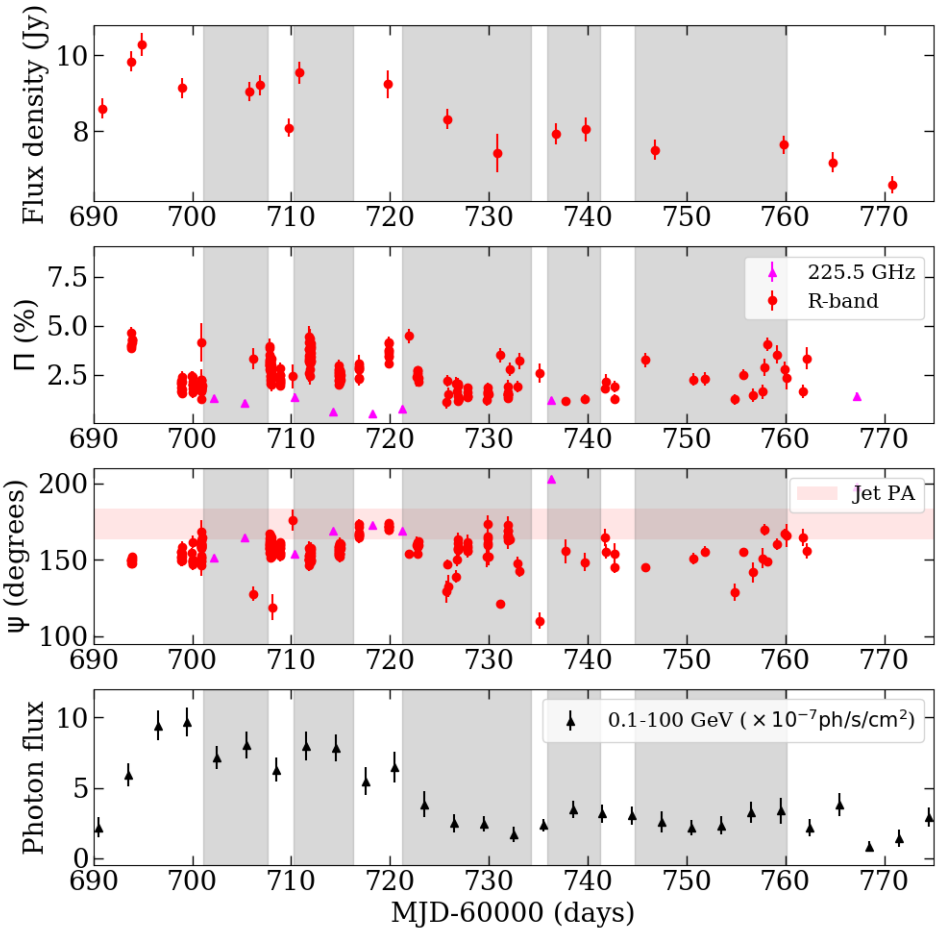

Figure 3. Multiwavelength brightness and polarization observation during the IXPE observations. The top panel shows the flux density in optical (*R* band), the second panel shows the host-corrected optical (*R* band) and millimeter radio (225.5 GHz) polarization degree (%), the third panel shows the optical and radio polarization angle (degrees), and the bottom panel shows the γ-ray photon flux 3-day binned light curves. The gray shaded areas mark the IXPE exposures over the entire observation. The horizontal red shaded area marks the projected direction of the jet. The error bars correspond to the 68% (1σ) confidence interval.

optical and radio telescopes. We also conducted several very long baseline interferometry (VLBI) observations using the VLBA through the MOJAVE (M. L. Lister et al. 2018)[45] and BEAM-ME (S. Jorstad & A. Marscher 2016)[46] programs that will be discussed separately in an upcoming publication (G. Paraschos et al. 2025, in preparation). The optical and radio observations are discussed in more detail in Appendix B. We also take advantage of the Fermi gamma-ray space telescope light-curve repository (S. Abdollahi et al. 2023) to extract the 3-day binned light curve. The *R*-band, millimeter radio (225.5 GHz), and γ-ray observations are shown in Figure 3. We focus on the highest available radio frequency since that is the least affected from Faraday effects and is likely in the optical thin regime as the optical and X-rays.

The optical, broadband, linear polarization shows rapid variability between $\sim$2% and 4% about the jet axis ($175° \pm 10°$; T. P. Krichbaum et al. 1992; H. Nagai et al. 2010; K. Suzuki et al. 2012; G. F. Paraschos et al. 2022). At the same time, the millimeter radio (225.5 GHz) shows milder variability at $\sim$1% also aligned with the jet axis. We find a strong correlation between the optical and γ-ray variability with a time lag of about zero (see Appendix B.2), consistent with typical behavior of blazars that indicates Compton scattering from relativistic electrons in the jet (I. Liodakis et al. 2018b, 2019; T. de Jaeger et al. 2023).

3. Discussion and Conclusions

We presented novel multiwavelength polarization observations of 3C 84 during a bright γ-ray flare. The unprecedented sensitivity of the IXPE observation allowed us to detect an X-ray polarization degree of $\Pi_X = 4.2\% \pm 1.3\%$ that is aligned with the jet axis. Previous IXPE observations of Seyfert 2–type galaxies such as 3C 84 show the opposite polarization behavior, i.e., a high Π_X that is perpendicular to the jet axis (F. Ursini et al. 2023; F. Marin et al. 2024). There is in fact now an emerging X-ray polarization unification picture where both stellar and supermassive obscured black holes show the same behavior (M. L. Saade et al. 2024). The tendency of 3C 84 to behave more like BL Lac–type objects has already been noted (P. Veron 1978) and was also found in our spectropolarimetric observations (F. Marin et al. 2025). This strongly rejects scattering on the dusty torus or on the polar winds as the origin of the X-ray polarization.

We also find a low yet strongly variable optical ($\Pi_O \sim 2\%$–4%) and radio ($\Pi_R \sim 1\%$) polarization degree that is also aligned with

[45] https://www.cv.nrao.edu/MOJAVE/index.html
[46] https://www.bu.edu/blazars/BEAM-ME.html

the jet. Given the orientation of the jet and the limited resolution of the optical and single-dish radio telescopes, the polarization degree is averaged over the entire jet with multiple emission regions with different magnetic field orientations likely depolarizing the observed emission. It is also likely that there is a minor contribution from the polar-scattered, inner thermal emission in the optical bands. However, the strong polarization variability and the overall blazar-like behavior lead us to conclude that the optical emission and radio emission are dominated by the jet, yet the intrinsic polarization is significantly depolarized in our limited resolution. This would suggest that the intrinsic radio and optical polarization degree (see also G. Paraschos et al. 2025, in preparation) is higher than the X-ray polarization degree. For flaring jets, as is the case for 3C 84, proton processes are expected to produce X-ray polarization at a similar level to the optical polarization (H. Zhang et al. 2024), in tension with our observation. Finally, we find a strong correlation between optical and γ-rays with a time lag of about zero as is typically expected from Compton scattering from relativistic electrons. That is true for not only the long-term behavior but also the flare in 2025 contemporaneous to our multiwavelength campaign (see Appendix B.2).

All of the above strongly point to Compton scattering from relativistic electrons in the jet as the origin of the X-ray emission. The fact that we detect any polarization is contrary to the expectations from external Compton scattering, where the target photon field is coming from structures external to the jet (e.g., accretion disk, broad-line region, torus, etc.; H. Zhang & M. Böttcher 2013; H. Zhang et al. 2024). Instead, it suggests synchrotron self-Compton likely taking place at parsec scales downstream from the black hole. A similar conclusion was reached for Cen A through multiwavelength modeling (F. Marin et al. 2023), suggesting that, similar to blazars (I. Liodakis et al. 2025), X-rays in radio galaxies are dominated by Compton scattering of seed photons coming from the jet.

Acknowledgments

The Imaging X-ray Polarimetry Explorer (IXPE) is a joint US and Italian mission. The US contribution is supported by the National Aeronautics and Space Administration (NASA) and led and managed by its Marshall Space Flight Center (MSFC), with industry partner Ball Aerospace (contract NNM15AA18C)—now, BAE Systems. The Italian contribution is supported by the Italian Space Agency (Agenzia Spaziale Italiana, ASI) through contract ASI-OHBI-2022-13-I.0, agreements ASI-INAF-2022-19-HH.0 and ASI-INFN-2017.13-H0, and its Space Science Data Center (SSDC) with agreements ASI-INAF-2022-14-HH.0 and ASI-INFN 2021-43-HH.0, and by the Istituto Nazionale di Astrofisica (INAF) and the Istituto Nazionale di Fisica Nucleare (INFN) in Italy. This research used data products provided by the IXPE Team (MSFC, SSDC, INAF, and INFN) and distributed with additional software tools by the High-Energy Astrophysics Science Archive Research Center (HEASARC), at NASA Goddard Space Flight Center (GSFC). Some of the data are based on observations collected at the Observatorio de Sierra Nevada, which is owned and operated by the Instituto de Astrofísica de Andalucía (IAA-CSIC), and at the Centro Astronómico Hispano en Andalucía (CAHA), which is operated jointly by Junta de Andalucía and Consejo Superior de Investigaciones Científicas (IAA-CSIC). The Perkins Telescope Observatory, located in Flagstaff, AZ, USA, is owned and operated by Boston University. This research was partially supported by the Bulgarian National Science Fund of the Ministry of Education and Science under grants KP-06-H68/4 (2022) and KP-06-H88/4 (2024). The data in this study include observations made with the Nordic Optical Telescope, owned in collaboration by the University of Turku and Aarhus University and operated jointly by Aarhus University, the University of Turku, and the University of Oslo, representing Denmark, Finland, and Norway, the University of Iceland, and Stockholm University at the Observatorio del Roque de los Muchachos, La Palma, Spain, of the Instituto de Astrofisica de Canarias. The data presented here were obtained in part with ALFOSC, which is provided by the Instituto de Astrofísica de Andalucía (IAA) under a joint agreement with the University of Copenhagen and NOT. The POLAMI observations reported here were carried out at the IRAM 30 m telescope. IRAM is supported by INSU/CNRS (France), MPG (Germany), and IGN (Spain). The Submillimeter Array (SMA) is a joint project between the Smithsonian Astrophysical Observatory and the Academia Sinica Institute of Astronomy and Astrophysics and is funded by the Smithsonian Institution and the Academia Sinica. Maunakea, the location of the SMA, is a culturally important site for the indigenous Hawaiian people; we are privileged to study the cosmos from its summit. The KVN is a facility operated by the Korea Astronomy and Space Science Institute. The KVN operations are supported by KREONET (Korea Research Environment Open NETwork), which is managed and operated by the Korea Institute of Science and Technology Information (KISTI). S.K., S.-S.L., W.Y.C., S.-H.K., and H.-W.J. were supported by the National Research Foundation of Korea (NRF) grant funded by the Korea government (MIST; 2020R1A2C2009003, RS-2025-00562700). Partly based on observations with the 100 m telescope of the Max-Planck-Institut für Radioastronomie (MPIfR) at Effelsberg. Observations with the 100 m radio telescope at Effelsberg have received funding from the European Union's Horizon 2020 research and innovation program under grant agreement No. 101004719 (ORP). The IAA-CSIC coauthors acknowledge financial support from the Spanish "Ministerio de Ciencia e Innovación" (MCIN/AEI/10.13039/501100011033) through the Center of Excellence Severo Ochoa award for the Instituto de Astrofíisica de Andalucía-CSIC (CEX2021-001131-S) and through grants PID2019-107847RB-C44 and PID2022-139117NB-C44. I.L. was funded by the European Union ERC-2022-STG—BOOTES—101076343. Views and opinions expressed are, however, those of the author(s) only and do not necessarily reflect those of the European Union or the European Research Council Executive Agency. Neither the European Union nor the granting authority can be held responsible for them. J.O.-S. acknowledges financial support from the project ref. AST22_00001_9 with funding from the European Union—NextGenerationEU, the Ministerio de Ciencia, Innovación y Universidades, Plan de Recuperación, Transformación y Resiliencia, the Consejería de Universidad, Investigación e Innovación from the Junta de Andalucía and the Consejo Superior de Investigaciones Científicas, and INFN Cap. U.1.01.01.01.009. This work has been partially supported by the ASI-INAF program I/004/11/4. The research at Boston University was supported in part by National Science Foundation grant AST-2108622, NASA Fermi Guest

Investigator grants 80NSSC23K1507 and 80NSSC23K1508, NASA NuSTAR Guest Investigator grant 80NSSC24K0547, and NASA Swift Guest Investigator grant 80NSSC23K1145. E.L. was supported by Academy of Finland projects 317636 and 320045. We acknowledge funding to support our NOT observations from the Finnish Centre for Astronomy with ESO (FINCA), University of Turku, Finland (Academy of Finland grant No. 306531). This research has made use of data from the MOJAVE database that is maintained by the MOJAVE team (M. L. Lister et al. 2018). Y.Y.K. was supported by the MuSES project, which has received funding from the European Union (ERC grant agreement No. 101142396). Views and opinions expressed are, however, those of the author(s) only and do not necessarily reflect those of the European Union or ERCEA. Neither the European Union nor the granting authority can be held responsible for them. This work has made use of data from the Joan Oró Telescope (TJO) of the Montsec Observatory (OdM), which is owned by the Catalan Government and operated by the Institute for Space Studies of Catalonia (IEEC). C.C. and D.A. acknowledge support from the European Research Council (ERC) under the Horizon ERC Grants 2021 program under grant agreement No. 101040021. The University of New Hampshire group is supported in part by NASA Astrophysics Astrophysics Data Analysis Program grant 80NSSC24K0636. We acknowledge support from NASA grant No. 80NSSC25K0002.

This research employs a list of Chandra data sets, obtained by the Chandra X-ray Observatory, contained in DOI:10.25574/cdc.487.

Facilities: IXPE, Swift (XRT), CXO, NuSTAR, Fermi, AO-B:0.6m, CAO:2.2 IRAM:30m, NOT, LX-200, Perkins, VLBA, OSN:0.9m, OSN:1.5m, SMA, KVN, Effelsberg.

Appendix A
X-Ray Polarization Data Analysis

Although the X-ray emission from 3C 84 itself is point-like, the thermal X-ray emission from the surrounding ICM is an astrophysical background that greatly complicates the analysis. Even in the case where the X-ray polarization of the ICM can be assumed to be exactly equal to zero a priori, properly disentangling the flux of the thermal and nonthermal AGN components is crucial for properly measuring the polarization degree and its statistical significance. Unfortunately, IXPE has neither the spatial nor spectral resolution to decisively separate these two components. The polarization signal we measure from 3C 84 over the course of these 2.5 Ms could also be contaminated by variations in the background, the AGN flux, or even changes in its polarization state. In this appendix, we describe the results of an extensive battery of tests to which the 3C 84 data were subjected to quantify the potential contribution of these intervening signals. All analysis of the IXPE data uses a combination of *ixpeobssim* version 31.1.0 (L. Baldini et al. 2022) and the IXPE analysis tools included with HEASoft v6.35.1 (Nasa High Energy Astrophysics Science Archive Research Center (Heasarc) 2014).

A.1. Astrophysical and Non-X-Ray Backgrounds

The long duration of this observation (approximately 2 months of wall-clock time from beginning to end) and the fact that these observations occurred near the peak of the solar cycle demand extra scrutiny for periods of high NXB event rates. The NXB component is independent of the astrophysical background and can vary strongly with time. This component is particularly important for IXPE data, for which the background has been found to show spurious polarization signals (N. Bucciantini et al. 2025; S. Silvestri et al. 2025, in preparation). We perform additional GTI filtering of the IXPE observations using light curves measured in the 8–10 keV band (i.e., outside the effective area bandpass of the IXPE mirrors). From these light curves (see Figure 4), we further filter out times of high activity. As this figure shows, the high rates observed in the 8–10 keV band correspond to similar flaring behavior in the 2–8 keV band. The first segment of the IXPE observation of Perseus also coincided with a period of enhanced γ-ray activity from 3C 84 (ATel 16998, 17020). We detect a flare in the 2–8 keV IXPE light curve in the first segment of observation, concurrent with a similar flare in 3–8 keV NuSTAR data (see Figure 5) and coincident with the period of renewed γ-ray activity. While there is little indication of significant spectral change during this flare and the total counts gathered during this flare are only a small fraction of the integrated signal, we nevertheless exclude it from our subsequent analysis.

In order to compare the relative contributions of the astrophysical background and NXB, we compare the surface brightness profile (see Figure 6) of the Perseus Cluster with an archival IXPE observation of a brighter point source MCG –5-23-16 (Obs ID 02003299), as well as a fainter source NGC 2110 (Obs ID 03008799). In the 8–10 keV band (where the mirrors have no effective area to X-ray photons), we find that the average count rates of both the Perseus Cluster and the point sources are similar outside of the central $\sim 1'$, showing that their NXB count rates are consistent with each other. When we instead consider the 2–8 keV band, we find that Perseus's surface brightness is at least a factor of 2 larger than the point sources at a distance of $6'$ from 3C 84. From these calculations we conclude that the astrophysical background dominates over the NXB throughout the entire usable field of view for the IXPE data. Near 3C 84 the astrophysical background is expected to be at least an order of magnitude higher than the inferred NXB.

Before we further test the spectropolarimetric fit for 3C 84, we have also performed a simple model-independent test of the polarization in the $2'$–$3'$ annular region just outside of 3C 84 using *ixpeobssim* 31.1.0[47] (L. Baldini et al. 2022). In this region, we find from Figure 7 that our polarization degree is $\sim$0.9% and a value of $\mathrm{MDP}_{99} = 1.8\%$. This provides strong and precise evidence that any polarization signal we measure for 3C 84 is not associated with the astrophysical background or NXB. A second model-independent test was performed after rotating the Stokes parameters for each event in this annulus with respect to its position relative to 3C 84. This rotation enables the possible detection of radial or azimuthal polarization structure that would otherwise average to zero net polarization geometrically. Similar to the first case, we find a polarization degree of 0.4% and $\mathrm{MDP}_{99} = 1.6\%$. When combined with the fact that the astrophysical background count rate in this region is more than an order of magnitude larger than the NXB count rate, we conclude that the NXB can be safely neglected in our spectropolarimetric fit.

[47] https://ixpeobssim.readthedocs.io/en/latest/

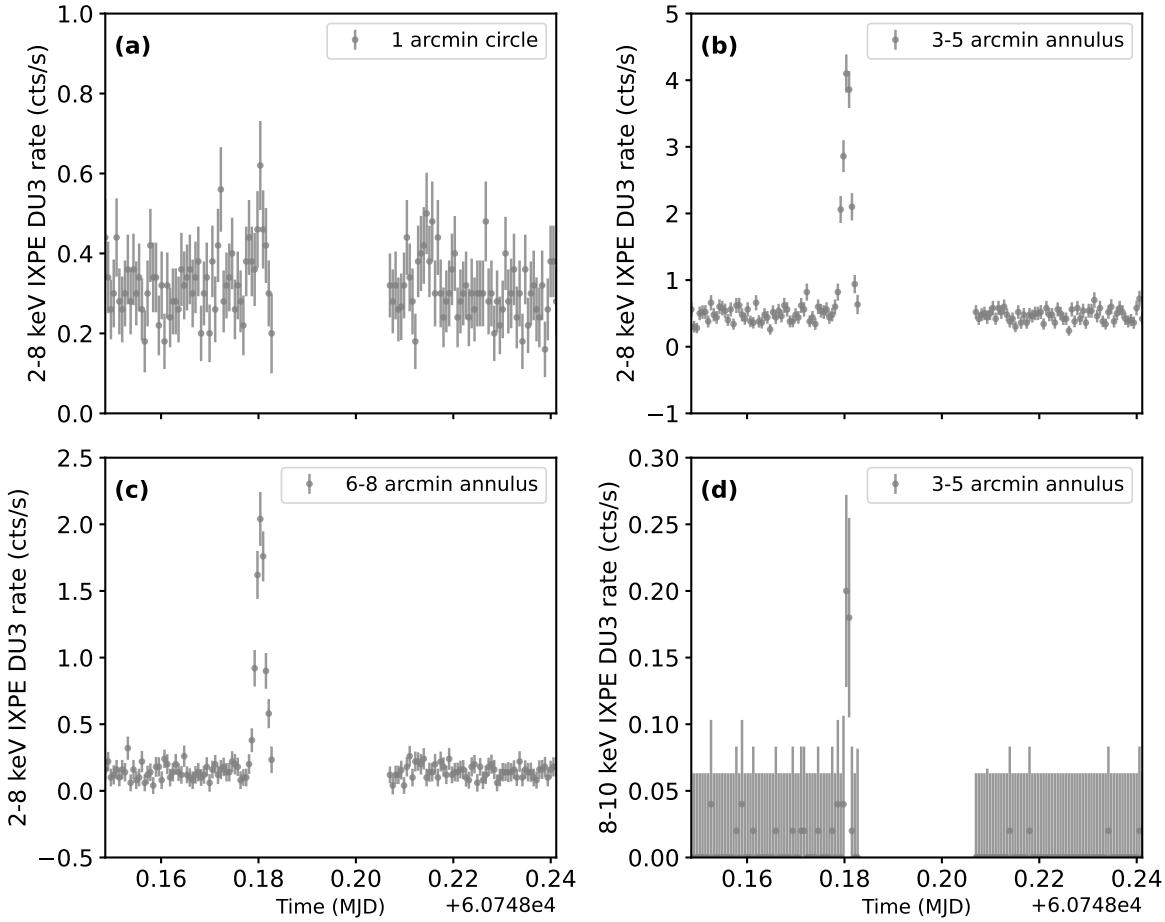

Figure 4. Example of a flare in the IXPE data, with the DU3 light curve as a reference. Panel (a) shows the 2–8 keV light curve from a 1′ circle centered around 3C 84. The flare is not obvious. Panels (b) and (c) show the light curve from the same time frame, but from the Perseus Cluster from annular regions between 3′–5′ and 6′–8′, respectively. The flare is much more prominent in the absence of 3C 84. Panel (d) shows the 3′–5′ light curve in 2–8 keV, outside the science window. The flare is still visible, indicating a likely nonastrophysical origin. In our subsequent analysis, we reject the flare times.

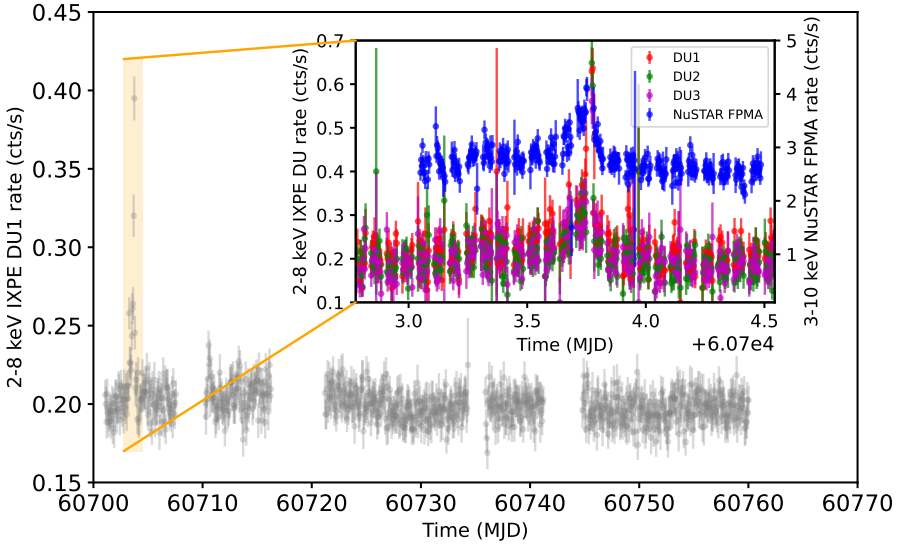

Figure 5. IXPE DU1 light curve of 3C 84 (in gray). The flare, shaded yellow, is observed simultaneously in all IXPE DUs (orange, green, and magenta light curves in the inset), as well as the simultaneous NuSTAR observation (blue light curve in the inset). This part of the light curve coincides with the period of enhanced activity from 3C 84.

Performing a similar model-independent polarization cube analysis for the 1′-radius circular region around 3C 84 results provides the first evidence of a statistically significant detection of X-ray polarization for this AGN. The resultant polarization cube measures a polarization degree of $\Pi_X = 2.42\% \pm 0.79\%$, corresponding to a $\sim 3\sigma$ detection. The polarization angle for this simple analysis is $\psi_X = 164.^{\circ}5 \pm 9.^{\circ}3$, which is consistent with being parallel to the radio jet.

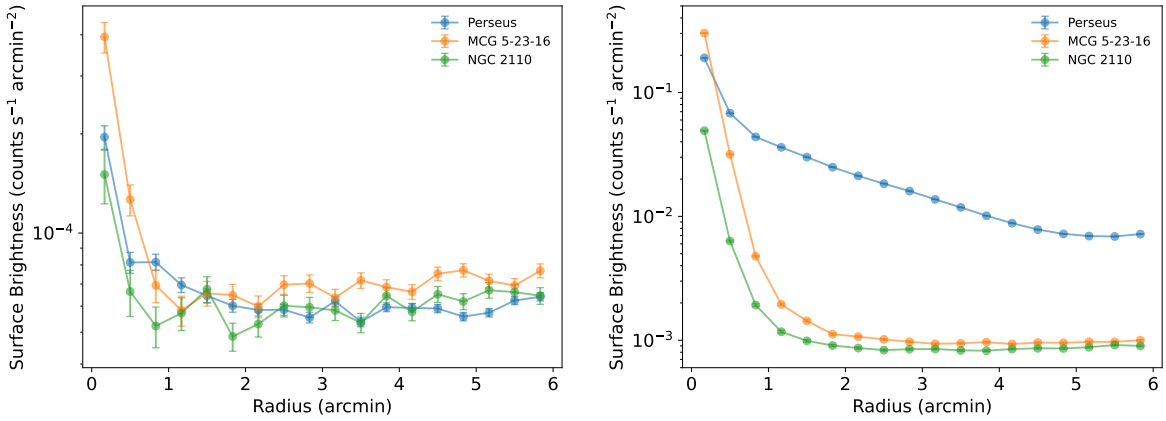

Figure 6. Surface brightness profiles of Perseus (blue) and two example point sources of different brightness, MCG –5-23-16 (orange) and NGC 2110 (green). Left panel: 8–10 keV surface brightness profiles. It demonstrates that the NXB levels are the same in all three IXPE observations. Right panel: the corresponding 2–8 keV surface brightness profiles. Even at distances as far away as 6′, Perseus is at least a factor of ∼6 brighter than the point sources. Together, these two panels imply that the cluster is observed throughout and the NXB is much less than the astrophysical background.

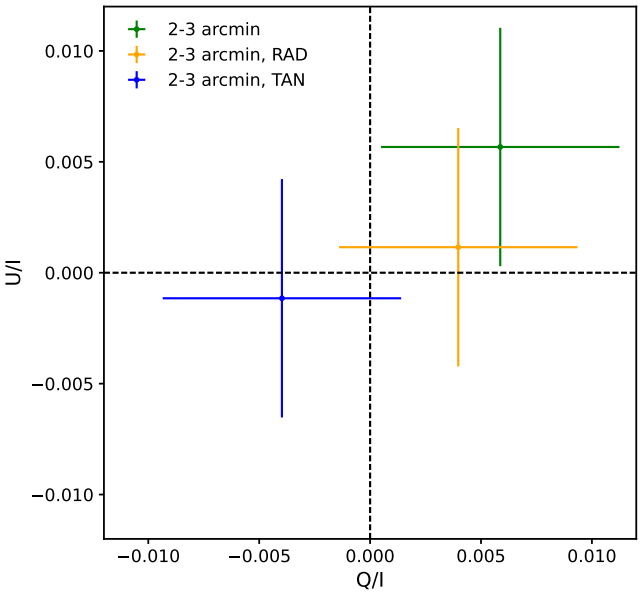

Figure 7. *Q*–*U* plot (green) for the 2′–3′ region of the Perseus Cluster in 2–8 keV, along with the corresponding values for Stokes rotation along the radial (orange) and azimuthal (blue) directions. This annular region is dominated by thermal emission from the ICM. The error bars are at the 1σ level. For all three cases, there is no evidence of significant polarization of the ICM photons.

A.2. Spectral Modeling for 3C 84 and the ICM

No single X-ray telescope can provide a complete and unambiguous spectral model for both 3C 84 and the surrounding ICM. In order to construct the most accurate model of the AGN plus ICM during our IXPE observations, we leverage existing observations of the Perseus Cluster with multiple X-ray telescopes to develop our joint model. After describing our rigorously derived spectral model for 3C 84 +ICM as observed with IXPE, we will discuss the sensitivity of the resultant polarimetric measurement to possible systematic errors arising from modeling deficiencies by considering a few extreme cases when compared to our fiducial model. These will ultimately show that the measured polarization signal is robust to systematic uncertainties in our joint model.

A.2.1. Chandra Observations

Our best constraints on the thermal properties of the ICM surrounding 3C 84 come from Chandra observation ID #4952 (carried out on 2004 October 14, with an exposure of 164.2 ks). This particular observation of the Perseus Cluster uses the ACIS-S detector, which minimizes systematics associated with the ACIS-I chip gaps that would be located in the regions of interest here. Unfortunately, Chandra observations show that 3C 84 itself suffers from pileup, making it impossible to extract an accurate spectrum of the AGN. We perform our analysis of the thermal spectrum using an annular region of 5″–30″ centered on 3C 84, where we expect point-like emission from 3C 84 to be negligible even in the presence of pileup.[48] All of our thermal models assume the abundance model of Wilms (J. Wilms et al. 2000), consistent with the study of the Perseus Cluster using Hitomi data (Hitomi Collaboration et al. 2017). Unless otherwise noted, all spectral fits are performed in the 0.5–7 keV band. The spectral and subsequent spectro-polarimetric analyses are carried out with HEASoft v6.35.1, and errors are stated at the 1σ confidence level.

Because this annular region is significantly larger than the Chandra point-spread function (PSF) and the annular binning used in past studies of the Perseus Cluster that study this same region (e.g., R. W. Schmidt et al. 2002; A. C. Fabian et al. 2006, 2011, 2017), we fit its spectrum using several models of varying complexity to account for possible multiphase emission. Past studies using Chandra observations have shown that subregions of our annular aperture are well described by a single thermal component with a temperature of $kT \sim 3$ keV (R. W. Schmidt et al. 2002; A. C. Fabian et al. 2006, 2011, 2017), but the additional photon statistics gained by our larger region may provide evidence of additional components. We find that a simple absorbed thermal model (`tbabs*apec` in XSPEC nomenclature) does not result in a formally acceptable fit to the data ($\chi^2 = 1038$ for 437 degrees of freedom (dof)). For this assumed emission model, clear residuals are seen around the emission lines at 1.2 and 2.3 keV. Motivated by the spectral model fit of a larger region of the Perseus Cluster with the Hitomi data (Hitomi Collaboration et al. 2017), we also

[48] See Figures 6.12 and 6.23 of the Chandra Proposer's Observatory Guide (https://cxc.harvard.edu/proposer/POG/html/chap6.html) for discussion of the Chandra on-axis PSF and how it varies with pileup.

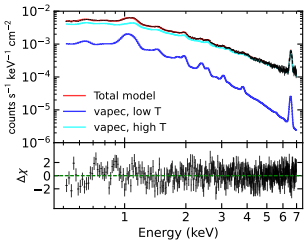

Figure 8. Chandra ACIS spectrum of the Perseus Cluster's thermal emission. We find a two-temperature model with low-temperature (1.65 keV) and high-temperature (4.39 keV) VAPEC components to be the best description of the 0.5–7 keV spectrum.

Table 1
Best-fit Spectral Parameters for 3C 84 and the Surrounding ICM Using a Combination of X-Ray Telescopes

Model	Parameters	Chandra	Swift/XRT +NuSTAR	IXPE
tbabs	$N_{\rm H}$ ($\times 10^{22}$ cm^{-2})	$0.176^{+0.001}_{-0.001}$	$0.188^{+0.012}_{-0.011}$	$0.184^{+0.011}_{-0.010}$
polconst	Π (%)	⋯	⋯	4.18 ± 1.31
	Ψ (deg)	⋯	⋯	$162.8^{+9.2}_{-9.1}$
powerlaw	Γ	⋯	$1.64^{+0.04}_{-0.04}$	$1.66^{+0.03}_{-0.03}$
	Norm	⋯	9.2×10^{-3}	3.6×10^{-2}
zgauss	Line energy (keV)	⋯	6.4^{f}	6.4^{f}
	Line width (keV)	⋯	0^{f}	0^{f}
	Norm	⋯	1.6×10^{-4}	2.2×10^{-5}
polconst$_0$	Π (%)	⋯	⋯	0^{f}
	Ψ (deg)	⋯	⋯	0^{f}
vapec$_1$	kT (keV)	$1.65^{+0.04}_{-0.10}$	1.65^{f}	1.65^{f}
	Norm	4.15×10^{-3}	5.56×10^{-2}	6.55×10^{-2}
vapec$_2$	kT (keV)	$4.39^{+0.09}_{-0.20}$	4.39^{f}	4.39^{f}
	Si	$1.67^{+0.06}_{-0.06}$	1.0^{f}	1.0^{f}
	S	$0.99^{+0.06}_{-0.06}$	1.0^{f}	1.0^{f}
	Ar	$1.16^{+0.17}_{-0.17}$	1.0^{f}	1.0^{f}
	Ca	$1.30^{+0.18}_{-0.18}$	1.0^{f}	1.0^{f}
	Fe	$0.87^{+0.02}_{-0.02}$	$0.50^{+0.02}_{-0.02}$	0.50^{f}
	Norm	1.93×10^{-2}	1.29×10^{-1}	1.29×10^{-1}
	χ^2/dof	498/434	1387/1357	2737/2690

Note. Chandra observations are used to constrain the two thermal components of the ICM, while the NuSTAR + Swift data are included to constrain 3C 84's power-law emission in conjunction with the Chandra-derived thermal emission model. Model: `tbabs*(polconst*(powerlaw+zgauss)+polconst$_0$(vapec$_1$+vapec$_2$))`.

consider a more complex two-component thermal model with free elemental abundances and intrinsic absorption (`tbabs*(vapec+vapec)`). We allow the abundances of Si, S, Ar, Ca, and Fe to vary freely with respect to the solar model, which are all free parameters in the Hitomi fit. Hitomi also allowed the Ni abundance as a free parameter, but given that these lines are predominantly above 8.0 keV, we do not allow it to vary freely here. The abundance values are tied to equal values for the two temperature components. The best-fit model has temperatures of $kT = 1.65^{+0.04}_{-0.09}$ keV and $kT = 4.39^{+0.09}_{-0.20}$ keV, respectively, along with supersolar abundances of Si, Ar, and Ca. These parameters are broadly consistent with the values measured in Hitomi and XMM-Newton, and we attribute the detailed differences between these parameters to the different spectral extraction regions and cross-calibration uncertainties associated with these two telescopes.[49] The addition of a second temperature and free elemental abundances greatly improves the overall quality of the fit, with a best-fit value of $\chi^2 = 498$ and 434 dof (see Figure 8 for the Chandra spectrum, along with the best-fit model). For completeness, we also consider a model where the thermal emission is a cooling flow from its upper temperature, again with free elemental abundances (`tbabs*(vapec+mkcflow)`) where the upper temperature of the cooling flow component is tied to the primary `apec` component, the metallicities of both components are tied to one another, and the normalization corresponds to a residual X-ray cooling flow. For this model, we find that the total cooling flow rate is $\dot{M} = 22 \pm 1.3 M_{\odot}$ yr^{-1} and the fit statistic is $\chi^2 = 664$ for 438 dof. We therefore conclude that this model fits the data significantly worse than our two-temperature model. Since this two-temperature model corresponds to a better overall fit and is further supported by the study of Hitomi, we choose the free elemental abundance model as our baseline for the spectro-polarimetric fit. This model, whose parameters are described in the Chandra column of Table 1, represents our fiducial thermal model.

A.2.2. NuSTAR and Swift Observations

While the Chandra observations are able to provide a clear measurement of the ICM's thermal properties without contamination from 3C 84, the presence of pileup makes it unable to characterize the emission of the AGN itself. To model the AGN's spectrum, we instead use Swift XRT + NuSTAR calibration observations of the Perseus Cluster taken simultaneously with the IXPE observations to characterize the flux and spectrum of 3C 84. Although the Swift + NuSTAR observations do not suffer the same limitations as Chandra for modeling the spectrum of 3C 84, we do expect the observed spectrum in our source aperture to include photons from the ICM and the AGN. The use of data from all three telescopes is therefore crucial for characterizing not only the AGN spectrum but also the relative flux contributions of the two components.

We reduce the NuSTAR data using NUSTARDAS v2.1.4 using default parameters, in conjunction with CALDB v20250224. We create a GTI file by weeding out the previously mentioned flare using XSELECT. Then, we extract the source photons using the NUPRODUCTS task from a 1′ region centered on the AGN, and we use a separate 1′ region far away from the source as the background region. We bin the spectrum to a minimum of 25 counts per bin for further XSPEC analysis. The effective NuSTAR exposure time was 45.3 ks for FPMA and 45.0 ks for FPMB.

Swift/XRT observed Perseus multiple times during the IXPE observation. Since all but one of these observations were carried out in WT mode, we exclusively use all the WT mode data during the span of the IXPE observation. We follow the standard extraction method from P. Evans et al. (2007) and P. A. Evans et al. (2009) and use the automated XRT product generation service.[50] In this, the cleaned event lists and

[49] For context, the Chandra region we have chosen is smaller than a single Hitomi SXS pixel (1′ × 1′), while the Hitomi result uses all of its 25 pixels for three overlapping but slightly offset pointings.
[50] https://www.swift.ac.uk/user_objects/

exposure maps per observation are using XRTPIPELINE, a box of 1′ length is selected around the source, and the entire window excluding a 120-pixel (283″) wide box centered on the source is designated as the background region. For each of the observations an appropriate ancillary response file (ARF) is generated using XRTMKARF and the corresponding exposure map. The cleaned event lists are then combined, and the combined source and background spectra are generated using XSELECT. ARFs are added using the ADDARF tool, and the BACKSCAL keyword is set appropriately. 3C 84 is not piled up in WT mode; hence, we do not need any further correction. The combined XRT spectrum had an exposure time of 2.4 ks.

We fit the Swift + NuSTAR data to our fiducial thermal model (two temperatures with free elemental abundances), a power-law component, and a redshifted Gaussian Fe Kα emission line. This emission line was found in E. Churazov et al. (2003) to be associated with 3C 84 itself, and while not visually obvious in our spectra, its inclusion nevertheless makes a significant improvement to the fit. Both the temperatures for our two thermal components are fixed to their Chandra-derived values, but their normalizations were allowed to be free parameters in the fit. This step is required to account for the fact that our NuSTAR + Swift data will inevitably sample different physical regions of the cluster given the variations in the PSF between these three telescopes.

Due to the much lower angular resolution of Swift/XRT and NuSTAR, contributions from farther-out gas could change the abundances relative to the Chandra values. In additiona to the much lower spectral resolution in this case renders the fit relatively insensitive to the abundances except the Fe abundance. Therefore, for the Swift+NuSTAR fit, we freeze the other abundances to the solar value, keeping only the Fe abundance free. We restrict our fit to the 0.5–10 keV band for the Swift data and the 3–50 keV band for the NuSTAR data. Our best-fit power-law model has $\Gamma = 1.64 \pm 0.04$, broadly similar to many values measured in the past. This model has a χ^2 value of 1387 for 1357 dof. We tried a variation of this model by including a second redshifted neutral hydrogen absorption component with zTBabs, but we found that the second component attains values similar to $N_{\rm H}$ as the Galactic component with little improvement to the overall fit and leads to degeneracies with the Galactic TBabs component. Therefore, we chose a single TBabs as our preferred model. We find the best-fit $N_{\rm H}$ of $(1.88^{+0.12}_{-0.11}) \times 10^{21}\,{\rm cm}^{-2}$ to be consistent with the total Galactic hydrogen column density derived using the method of R. Willingale et al. (2013).[51] We also find a best-fit Fe abundance of 0.50 ± 0.02. The fluxes of 3C 84 and the ICM in the 2–8 keV band are 6.6×10^{-11} erg cm^{-2} s^{-1} and 7.5×10^{-11} erg cm^{-2} s^{-1}, respectively, suggesting that the ICM should contribute ∼53% of the photons observed in the IXPE aperture. The equivalent width of the Gaussian line is found to be 77.7 eV.

A.3. Spectropolarimetric Fit with IXPE

Based on the surface brightness profiles mentioned in Appendix A.1, we take the average 2–8 keV surface brightness profiles of MCG –5-23-16 and NGC 2110, scaled to match the o n-axis count rate of Perseus, as a template for a point source at this flux level, and we compare it with the 2–8 keV surface brightness profile of Perseus. This gives us an idea of the relative contribution between the power-law component from 3C 84 and the thermal components from the cluster gas, as a function of the off-axis radius. We find that beyond ∼40″ the cluster dominates over the AGN contribution, thereby diluting the 3C 84 polarization and adding degeneracies. We therefore chose a source extraction region below this value, 30″ in radius or about two times the in-orbit half-power diameter of IXPE to be precise. We keep the normalizations of the power-law and vapec components free in the subsequent spectropolarimetric fits to account for a different AGN/cluster flux ratio.

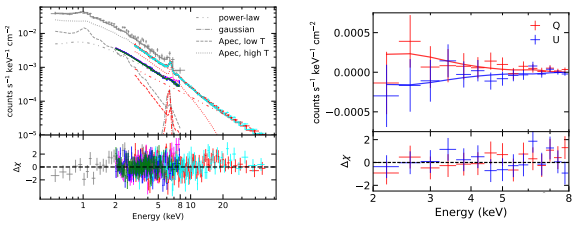

Figure 9. Spectropolarimetric fit between Swift/XRT, NuSTAR, and IXPE. The left panel shows the 0.5–50 keV spectral fit, with XRT in gray; IXPE DUs in magenta, blue, and green; and NuSTAR FPMA and FPMB in red and cyan, respectively. The best-fit model consists of an absorbed power law, a narrow Gaussian at Fe K energies, and a two-temperature thermal model based on our Chandra fit. The right panel shows the corresponding fit for the Q and U spectra. We have shown the fit for only the DU1 for greater clarity. We assumed a constant polarization model for the fit.

The combination of Chandra, Swift, and NuSTAR observations provides us with a complete spectral model that we will use to measure the polarization of 3C 84. The full spectral model is found in Table 1 and includes both our fiducial thermal model from the Chandra observations and our power-law + Gaussian model from the Swift + NuSTAR fit. We fit the IXPE, NUSTAR, and Swift data simultaneously in our spectropolarimetric fit (see Figure 9). To maximize polarization sensitivity, we use the $N_{\rm eff}$ weighting for the polarimetric data. None of the key free parameters of this complex model fit differ significantly from their best-fit values to the Swift+NuSTAR fit described above, with all parameter values within 1σ of one another. We find that the best-fit polarization degree is $\Pi_{\rm X} = 4.18\% \pm 1.31\%$ and the best-fit angle is $\psi_{\rm X} = 162.^{\circ}8 \pm 9.^{\circ}2$. This corresponds to a detection at the $\sim 3.2\sigma$ level and a polarization angle approximately parallel to the jet.

Further testing of this spectropolarimetric fit shows that this polarization degree is not sensitive to the particulars of the thermal background model. If we instead choose a simpler single-temperature thermal model for the ICM, we get a similar fit quality to the Swift + NuSTAR + IXPE spectra and a polarization degree of $\Pi_{\rm X} = 3.51\% \pm 1.12\%$ and $\psi_{\rm X} = 162.^{\circ}4 \pm 9.^{\circ}3$. Even under the extreme and absurd assumption that the entire IXPE spectrum originates from a single power-law component, we measure a polarization degree of $\Pi_{\rm X} = 3.1\% \pm 0.88\%$ and $\psi_{\rm X} = 165^{\circ} \pm 7^{\circ}$. With these tests, we have shown that our measured polarization degree is robust to the full range of physically feasible thermal emission models.

The Gaussian line is found to be faint in IXPE, with an equivalent width of ∼7 eV. If we fix the equivalent width of the Gaussian line in IXPE to the NuSTAR+XRT equivalent width, the fit quality remains relatively unchanged, with a $\chi^2/{\rm dof} = 2741/2690$, $\Pi_{\rm X} = 4.2\% \pm 1.3\%$, and $\psi_{\rm X} = 162.^{\circ}8 \pm 9.^{\circ}2$. The origin of the Gaussian line, however, is debated. Hitomi Collaboration et al. (2018) argue that the Gaussian might be coming from scattering off of a torus. Irrespective of the origin, though, as the Gaussian is rather weak in the IXPE data, assigning a polarization of 0 to it does not change our results.

[51] https://www.swift.ac.uk/analysis/nhtot/

We still get a $\chi^2/\mathrm{dof} = 2737/2690$, $\Pi_X = 4.16\% \pm 1.31\%$, and $\psi_X = 162.^{\circ}8 \pm 9.^{\circ}2$. This further demonstrates the robustness of our polarization measurement to any systematic uncertainty in the emission line.

Although we find that our Swift + NuSTAR spectrum is well fit by a single power law, we further test the possible presence of Compton scattering from a corona by fitting these spectral data to a nonthermal coronal Compton scattering (specifically the `Nthcomp` model in XSPEC; A. P. Lightman & A. A. Zdziarski 1987). We fix the seed photon spectrum to a disk blackbody spectrum with $kT_{\rm bb} = 100$ eV. We find that the best-fit `Nthcomp` model has a power-law index of $\Gamma = 1.67 \pm 0.03$, similar to what we measure for our simple power-law model. These data cannot directly measure the corona electron temperature, finding a lower limit of $kT_e > 455$ keV. Just as importantly, the overall fit statistic between the best-fit power-law and `Nthcomp` models are practically indistinguishable (χ^2/dof of $1387/1357$ for the power law vs. $1386/1356$ for `Nthcomp`). The spectral data are therefore unable to favor either the jet-dominated or corona-dominated origins for the X-rays. This is not surprising, as past studies have argued for both origins (e.g., V. Chitnis et al. 2020; C. S. Reynolds et al. 2021). The nearly identical predictions between the two models further emphasize the power of X-ray polarimetry to break the long-standing degeneracy between these two different physical models for the X-rays.

A.4. Tests for Polarization Variability

With a $\sim 3\sigma$ detection of X-ray polarization over such a long exposure, we further investigate the polarization data to see whether there is any evidence for time variability in the polarization signal. We calculate the average Stokes parameters for each of the five observation segments and perform the same analysis as in L. Di Gesu et al. (2023) and S. R. Ehlert et al. (2023) to test the null hypothesis that the average Stokes parameters in each observation segment are consistent with the time-integrated average. The χ^2 value for the time-resolved Stokes parameters is 11.5 with $2N - 2 = 8$ dof. This χ^2 value is not large enough to reject the null hypothesis of the Stokes parameters being constant throughout the entire exposure. We therefore conclude that the IXPE data are consistent with a constant polarization degree and angle throughout the exposure.

A.5. Test for Energy Dependence of Polarization

We further investigated the energy dependence of the polarization using the energy bands of 2–4 keV, 4–6 keV, and 6–8 keV. We carried out a methodology similar to the variability mentioned above by comparing the average polarization degree across the integrated 2–8 keV to those measured in these smaller energy bands. We find that the Stokes Q–U parameters for an assumed constant value with energy give a χ^2 of 4.66 with $2N - 2 = 4$ dof.

As a second independent test, we have also fit the IXPE +NuSTAR+Swift/XRT spectra with the `pollin` model in XSPEC, which assumes a constant + linear polarization degree and angle as a function of energy. We assume no change of the PA with energy, fixing that slope to be 0. Our best-fit value for the polarization degree slope is $A_{\Pi} = 0.01 \pm 0.01$, consistent with a constant polarization degree. The overall fit quality (`pollin` model, $\chi^2/\mathrm{dof} = 2736/2689$) is nearly identical to the fit quality of the model where we assume a constant polarization degree (`polconst` model, $\chi^2/\mathrm{dof} = 2737/2690$). With these two results, we conclude that there is no statistically significant evidence that the polarization degree changes with energy.

Appendix B
Radio and Optical Observations

Here we further discuss the contemporaneous radio, optical, and archival optical observations.

B.1. Polarization Observations

Optical observations covering the IXPE observation were taken using multiple telescopes across Europe and the United States. Those were namely the Belogradchik Observatory in Bulgaria (R. Bachev et al. 2023), the Calar Alto Observatory (J. Escudero Pedrosa et al. 2024a, 2024b) and Sierra Nevada Observatory (J. Otero-Santos et al. 2024) in continental Spain, the Nordic Optical Telescope (MAGIC Collaboration et al. 2018; K. Nilsson et al. 2018) in La Palma, Spain, the LX-200 in Russia, and the Perkins Telescope (S. G. Jorstad et al. 2010) in the United States. All the observations were reduced following standard polarimetric procedures and corrected for instrumental polarization using unpolarized and polarized standard stars. More details on the observations, data reduction, and observing strategies of the individual observatories can be found in previous IXPE-collaboration-led publications (e.g., L. Di Gesu et al. 2022; I. Liodakis et al. 2022; A. L. Peirson et al. 2023; P. M. Kouch et al. 2024).

3C 84 has a prominent host galaxy that contributes a significant fraction of unpolarized light. This depolarizing effect is taken into account in broadband measurements by

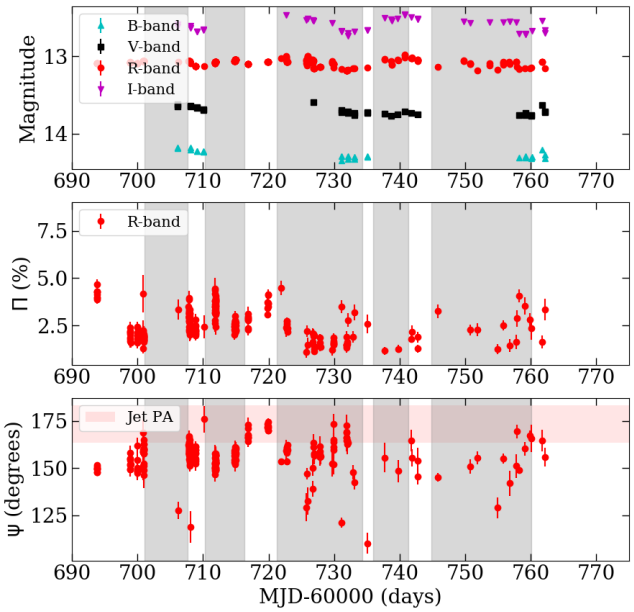

Figure 10. Optical brightness and polarization measurements during the IXPE observations. The top panel shows the brightness in magnitudes for different optical bands (*BVRI*), the middle panel the host-corrected polarization degree (%, *R* band), and the bottom panel the polarization angle (degrees, *R* band). The gray shaded areas mark the IXPE exposures over the entire observation. The different optical bands are marked with different symbols and colors as shown in the legend. The horizontal red shaded area marks the projected direction of the jet. The error bars correspond to the 68% (1σ) confidence interval.

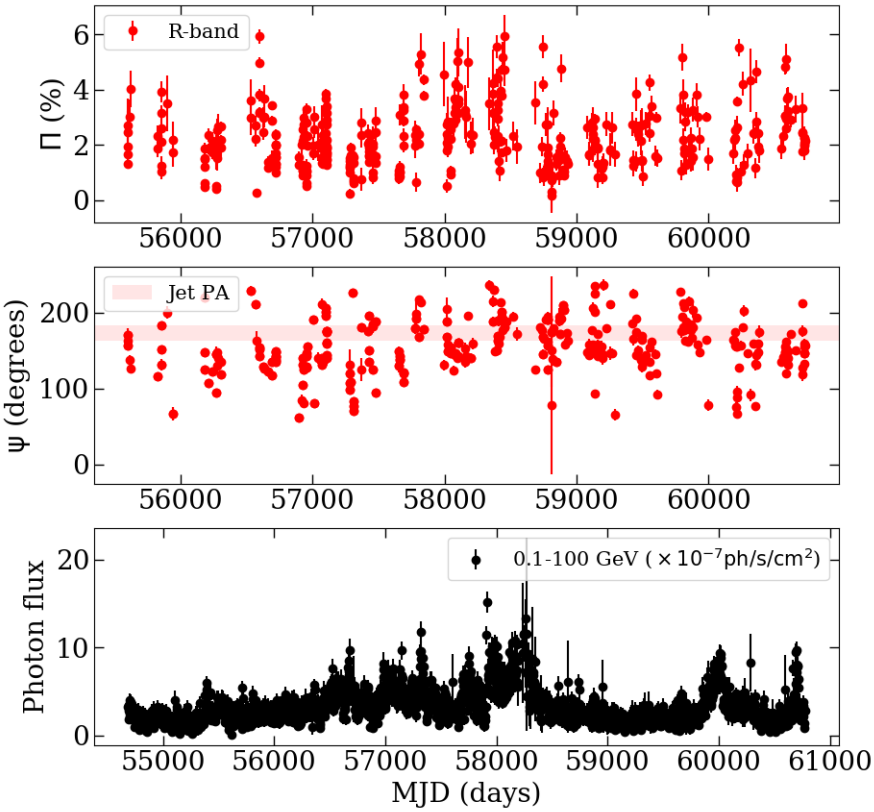

Figure 11. Archival optical and γ-ray polarization observations. The top panel shows the host-corrected polarization degree (%, *R* band), the middle panel the polarization angle (degrees, *R* band), and the bottom panel the 3-day binned Fermi photon flux light curve in the 0.1–100 GeV band. The horizontal red shaded area marks the projected direction of the jet. The error bars correspond to the 68% (1σ) confidence interval.

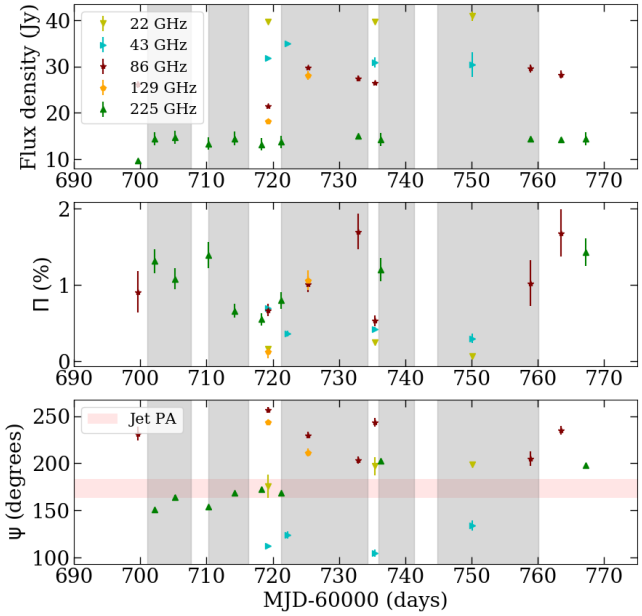

Figure 12. Radio flux density and polarization measurements during the IXPE observations. The top panel shows the flux density in jansky, the middle panel the polarization degree (%), and the bottom panel the polarization angle (degrees). The gray shaded areas mark the IXPE exposures over the entire observation. The different radio frequencies are marked with different symbols and colors as shown in the legend. The horizontal red shaded area marks the projected direction of the jet. The error bars correspond to the 68% (1σ) confidence interval.

making a model of the host galaxy light distribution (as in K. Nilsson et al. 2007) and estimating the flux density contribution of the host and Hα line (see J. Aleksić et al. 2014) to the aperture used for the individual observatories. That contribution is then subtracted from the total light, and the observed polarization degree is corrected following T. Hovatta et al. (2016). The intrinsic *R*-band polarization degree is plotted in Figure 10. Spectropolarimetry taken with the Nordic Optical Telescope is presented in an accompanying publication (F. Marin et al. 2025). In addition, we obtained archival optical polarization data from the Boston University monitoring program (now called BEAM-ME) to compare with the measurements obtained during the IXPE observation. We find a consistent behavior where the polarization degree varies from 2% to 4%, aligned with the jet direction (Figure 11).

In radio, 3C 84 was observed in nine frequencies from 2.5 to 225.5 GHz using the Effelsberg 100 m telescope as part of the Monitoring the Stokes *Q*, *U*, *I* and *V* Emission of AGN jets in Radio (QUIVER) program (2.5, 4.8, 8.3, 10.4 GHz; A. Kraus et al. 2003; I. Myserlis et al. 2018, 2025); the Korean VLBI Network (S. Kang et al. 2015) in single-dish mode (22, 43, 86, 129 GHz); the IRAM 30 m telescope through the Polarimetric Monitoring of AGN at Millimeter Wavelengths (I. Agudo et al. 2018) program (86, 225 GHz); and the SMA Monitoring of AGNs with Polarization (SMAPOL) program (225 GHz, I. Myserlis et al. 2025) using the Submillimeter Array. The radio observations are shown in Figure 12.

B.2. Cross-correlation Analysis

To probe the optical–γ-ray connection, we use contemporaneous and archival data from the Tuorla Monitoring program (K. Nilsson et al. 2018).[52] The observations are taken in the R band and are corrected for the host galaxy contribution, revealing a blazar-like light curve with several flares that appear to be well aligned with the γ-ray flares observed by Fermi. To better quantify the optical–γ-ray connection, we use the discrete correlation function (DCF; R. A. Edelson & J. H. Krolik 1988). We find a strong correlation between the long-term optical and γ-ray light curves with a time lag that is consistent with zero (8 ± 7 days; Figure 13, top panel). We repeated the analysis considering only the observations of the flare in 2025 that was contemporaneous with the IXPE observation. Similar to the long-term behavior, we also find the time lag to be consistent with zero (10 ± 6 days; Figure 13, top panel), suggesting that optical and γ-rays are emitted cospatially in both cases as expected from inverse Compton scattering.

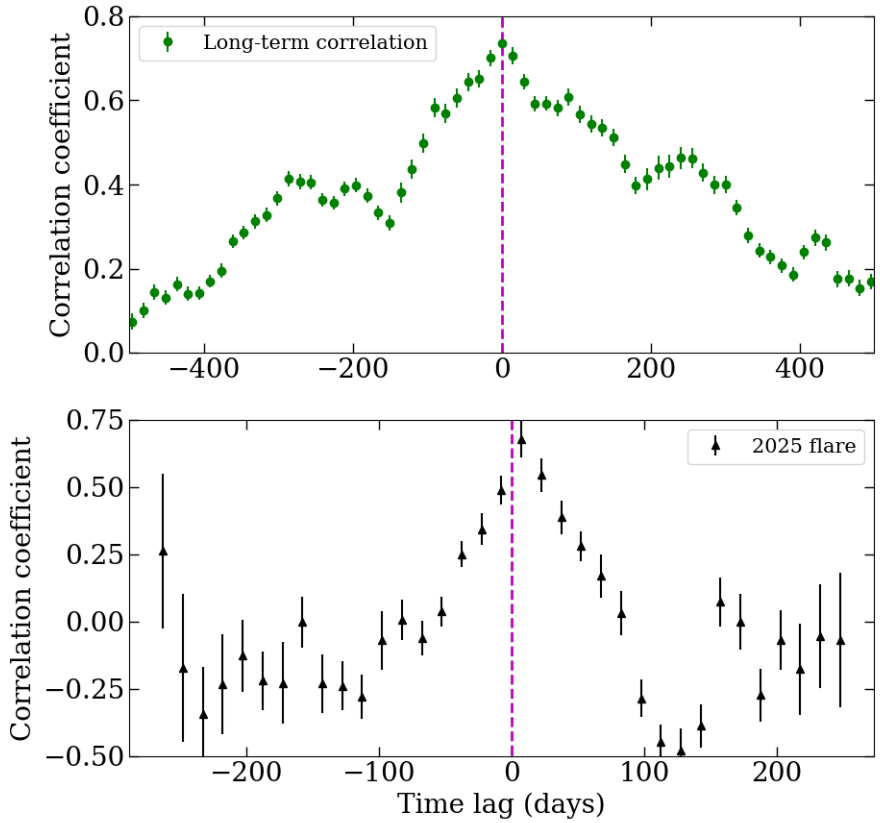

Figure 13. DCF between optical and the 3-day binned γ-ray light curves. The top panel shows the DCF considering all the available observations, and the bottom panel shows the DCF for the 2025 flare that coincided with the IXPE observations. In both panels the vertical magenta line marks a time lag of zero.

[52] https://tuorlablazar.utu.fi/

ORCID iDs

Ioannis Liodakis https://orcid.org/0000-0001-9200-4006
Frédéric Marin https://orcid.org/0000-0003-4952-0835
Steven R. Ehlert https://orcid.org/0000-0003-4420-2838
Thibault Barnouin https://orcid.org/0000-0003-1340-5675
Pouya M. Kouch https://orcid.org/0000-0002-9328-2750
Kari Nilsson https://orcid.org/0000-0002-1445-8683
Elina Lindfors https://orcid.org/0000-0002-9155-6199
Tapio Pursimo https://orcid.org/0000-0002-5578-9219
Georgios F. Paraschos https://orcid.org/0000-0001-6757-3098
Riccardo Middei https://orcid.org/0000-0001-9815-9092
Anna Trindade Falcão https://orcid.org/0000-0001-8112-3464
Svetlana Jorstad https://orcid.org/0000-0001-6158-1708
Iván Agudo https://orcid.org/0000-0002-3777-6182
Yuri Y. Kovalev https://orcid.org/0000-0001-9303-3263
Jacob J. Casey https://orcid.org/0009-0009-3051-6570
Laura Di Gesu https://orcid.org/0000-0002-5614-5028
Philip Kaaret https://orcid.org/0000-0002-3638-0637
Dawoon E. Kim https://orcid.org/0000-0001-5717-3736
Fabian Kislat https://orcid.org/0000-0001-7477-0380
Ajay Ratheesh https://orcid.org/0000-0003-0411-4243
M. Lynne Saade https://orcid.org/0000-0001-7163-7015
Francesco Tombesi https://orcid.org/0000-0002-6562-8654
Alan Marscher https://orcid.org/0000-0001-7396-3332
Giacomo Bonnoli https://orcid.org/0000-0003-2464-9077
Víctor Casanova https://orcid.org/0000-0003-2036-8999
Juan Escudero Pedrosa https://orcid.org/0000-0002-4131-655X
Daniel Morcuende https://orcid.org/0000-0001-9400-0922
Jorge Otero-Santos https://orcid.org/0000-0002-4241-5875
Vilppu Piirola https://orcid.org/0000-0003-0186-206X
Rumen Bachev https://orcid.org/0000-0002-0766-864X
George A. Borman https://orcid.org/0000-0002-7262-6710
Tatiana S. Grishina https://orcid.org/0000-0002-3953-6676
Vladimir A. Hagen-Thorn https://orcid.org/0000-0002-6431-8590
Evgenia N. Kopatskaya https://orcid.org/0000-0001-9518-337X
Elena G. Larionova https://orcid.org/0000-0002-2471-6500
Daria A. Morozova https://orcid.org/0000-0002-9407-7804
Sergey S. Savchenko https://orcid.org/0000-0003-4147-3851
Ekaterina V. Shishkina https://orcid.org/0009-0002-2440-2947
Ivan S. Troitskiy https://orcid.org/0000-0002-4218-0148
Yulia V. Troitskaya https://orcid.org/0000-0002-9907-9876
Andrey A. Vasilyev https://orcid.org/0000-0002-8293-0214
Ioannis Myserlis https://orcid.org/0000-0003-3025-9497
Mark Gurwell https://orcid.org/0000-0003-0685-3621
Garrett Keating https://orcid.org/0000-0002-3490-146X
Ramprasad Rao https://orcid.org/0000-0002-1407-7944
Sincheol Kang https://orcid.org/0000-0002-0112-4836
Sang-Sung Lee https://orcid.org/0000-0002-6269-594X
Sanghyun Kim https://orcid.org/0000-0001-7556-8504
Whee Yeon Cheong https://orcid.org/0009-0002-1871-5824
Hyeon-Woo Jeong https://orcid.org/0009-0005-7629-8450
Chanwoo Song https://orcid.org/0009-0003-8767-7080
Shan Li https://orcid.org/0009-0006-1247-0976
Myeong-Seok Nam https://orcid.org/0009-0001-4748-0211
Diego Álvarez-Ortega https://orcid.org/0000-0002-9998-5238
Carolina Casadio https://orcid.org/0000-0003-1117-2863
Emmanouil Angelakis https://orcid.org/0000-0001-7327-5441
Alexander Kraus https://orcid.org/0000-0002-4184-9372
Jenni Jormanainen https://orcid.org/0000-0003-4519-7751
Vandad Fallah Ramazani https://orcid.org/0000-0001-8991-7744
Chien-Ting Chen https://orcid.org/0000-0002-4945-5079
Enrico Costa https://orcid.org/0000-0003-4925-8523
Riccardo Ferrazzoli https://orcid.org/0000-0003-1074-8605
Ildar Khabibullin https://orcid.org/0000-0003-3701-5882
Stephen L. O'Dell https://orcid.org/0000-0002-1868-8056
Luigi Pacciani https://orcid.org/0000-0001-6897-5996
Oliver J. Roberts https://orcid.org/0000-0002-7150-9061
Paolo Soffitta https://orcid.org/0000-0002-7781-4104
Douglas A. Swartz https://orcid.org/0000-0002-2954-4461
Fabrizio Tavecchio https://orcid.org/0000-0003-0256-0995
Martin C. Weisskopf https://orcid.org/0000-0002-5270-4240
Irina Zhuravleva https://orcid.org/0000-0001-7630-8085

References

Abdo, A. A., Ackermann, M., Ajello, M., et al. 2009, ApJ, 699, 31
Abdollahi, S., Ajello, M., Baldini, L., et al. 2023, ApJS, 265, 31
Agudo, I., Liodakis, I., Otero-Santos, J., et al. 2025, ApJ, 985, L15
Agudo, I., Thum, C., Molina, S. N., et al. 2018, MNRAS, 474, 1427
Aleksić, J., Ansoldi, S., Antonelli, L. A., et al. 2014, A&A, 564, A5
Antonucci, R. 1993, ARA&A, 31, 473
Bachev, R., Tripathi, T., Gupta, A. C., et al. 2023, MNRAS, 522, 3018
Baldini, L., Bucciantini, N., Lalla, N. D., et al. 2022, SoftX, 19, 101194
Böttcher, M., Reimer, A., Sweeney, K., & Prakash, A. 2013, ApJ, 768, 54
Bucciantini, N., Wong, J., Romani, R. W., et al. 2025, A&A, 699, A33
Cao, Z., Aharonian, F., Axikegu, et al. 2024, MNRAS, 540, 1860
Capecchiacci, S., Liodakis, I., Middei, R., et al. 2025, arXiv:2508.14168
Chakraborty, S., Ratheesh, A., Tagliacozzo, D., et al. 2025, ApJ, 990, 89
Chen, C.-T. J., Liodakis, I., Middei, R., et al. 2024, ApJ, 974, 50
Chitnis, V., Shukla, A., Singh, K. P., et al. 2020, Galax, 8, 63
Churazov, E., Forman, W., Jones, C., & Böhringer, H. 2003, ApJ, 590, 225
de Jaeger, T., Shappee, B. J., Kochanek, C. S., et al. 2023, MNRAS, 519, 6349
Di Gesu, L., Donnarumma, I., Tavecchio, F., et al. 2022, ApJL, 938, L7
Di Gesu, L., Marshall, H. L., Ehlert, S. R., et al. 2023, NatAs, 7, 1245
Di Marco, A., Soffitta, P., Costa, E., et al. 2023, AJ, 165, 143
Edelson, R. A., & Krolik, J. H. 1988, ApJ, 333, 646
Ehlert, S. R., Ferrazzoli, R., Marinucci, A., et al. 2022, ApJ, 935, 116
Ehlert, S. R., Liodakis, I., Middei, R., et al. 2023, ApJ, 959, 61
Escudero Pedrosa, J., Agudo, I., Morcuende, D., et al. 2024a, AJ, 168, 84
Escudero Pedrosa, J., Morcuende Parrilla, D., & Otero-Santos, J. 2024b, IOP4, v1.2.0, Zenodo, doi:10.5281/zenodo.10222722
Evans, P., Beardmore, A. P., Page, K. L., et al. 2007, A&A, 469, 379
Evans, P. A., Beardmore, A. P., Page, K. L., et al. 2009, MNRAS, 397, 1177
Fabian, A. C., Sanders, J. S., Allen, S. W., et al. 2011, MNRAS, 418, 2154
Fabian, A. C., Sanders, J. S., Taylor, G. B., et al. 2006, MNRAS, 366, 417
Fabian, A. C., Walker, S. A., Russell, H. R., et al. 2017, MNRAS, 464, L1
Fukazawa, Y., Shiki, K., Tanaka, Y., et al. 2018, ApJ, 855, 93
Gianolli, V. E., Kim, D. E., Bianchi, S., et al. 2023, MNRAS, 523, 4468
Giovannini, G., Savolainen, T., Orienti, M., et al. 2018, NatAs, 2, 472
Haardt, F., & Maraschi, L. 1991, ApJL, 380, L51
Hitomi Collaboration, Aharonian, F., Akamatsu, H., et al. 2017, Natur, 551, 478
Hitomi Collaboration, Aharonian, F., Akamatsu, H., et al. 2018, PASJ, 70, 13
Hodgson, J. A., Rani, B., Lee, S.-S., et al. 2018, MNRAS, 475, 368
Hodgson, J. A., Rani, B., Oh, J., et al. 2021, ApJ, 914, 43
Hovatta, T., Lindfors, E., Blinov, D., et al. 2016, A&A, 596, A78
Imazato, F., Fukazawa, Y., Sasada, M., & Sakamoto, T. 2021, ApJ, 906, 30

Ingram, A., Ewing, M., Marinucci, A., et al. 2023, MNRAS, 525, 5437
Jorstad, S., & Marscher, A. 2016, Galax, 4, 47
Jorstad, S. G., Marscher, A. P., Larionov, V. M., et al. 2010, ApJ, 715, 362
Kang, S., Lee, S.-S., & Byun, D.-Y. 2015, JKAS, 48, 257
Kara, E., Alston, W. N., Fabian, A. C., et al. 2016, MNRAS, 462, 511
Khachikian, E. Y., & Weedman, D. W. 1974, ApJ, 192, 581
Kim, J. Y., Krichbaum, T. P., Marscher, A. P., et al. 2019, A&A, 622, A196
Kouch, P. M., Liodakis, I., Fenu, F., et al. 2025, A&A, 695, A99
Kouch, P. M., Liodakis, I., Middei, R., et al. 2024, A&A, 689, A119
Kraus, A., Krichbaum, T. P., Wegner, R., et al. 2003, A&A, 401, 161
Krichbaum, T. P., Witzel, A., Graham, D. A., et al. 1992, A&A, 260, 33
Lightman, A. P., & Zdziarski, A. A. 1987, ApJ, 319, 643
Liodakis, I., Hovatta, T., Huppenkothen, D., et al. 2018a, ApJ, 866, 137
Liodakis, I., Marscher, A. P., Agudo, I., et al. 2022, Natur, 611, 677
Liodakis, I., Romani, R. W., Filippenko, A. V., Kocevski, D., & Zheng, W. 2019, ApJ, 880, 32
Liodakis, I., Romani, R. W., Filippenko, A. V., et al. 2018b, MNRAS, 480, 5517
Liodakis, I., Zhang, H., Boula, S., et al. 2025, A&A, 698, L19
Lister, M. L., Aller, M. F., Aller, H. D., et al. 2018, ApJS, 234, 12
MAGIC Collaboration, Ansoldi, S., Antonelli, L. A., et al. 2018, MNRAS, 480, 879
Mannheim, K. 1993, A&A, 269, 67
Marin, F., Barnouin, T., Ehlert, S. R., et al. 2023, MNRAS, 526, 6321
Marin, F., Marinucci, A., Laurenti, M., et al. 2024, A&A, 689, A238
Marin, F., Pursimo, T., Liodakis, I., et al. 2025, A&A, 702, L16
Marshall, H. L., Liodakis, I., Marscher, A. P., et al. 2024, ApJ, 972, 74
Mastichiadis, A. 1996, SSRv, 75, 317
Mastichiadis, A., & Kirk, J. G. 1997, A&A, 320, 19
Mastichiadis, A., & Petropoulou, M. 2021, ApJ, 906, 131
Middei, R., Liodakis, I., Perri, M., et al. 2023a, ApJL, 942, L10
Middei, R., Perri, M., Puccetti, S., et al. 2023b, ApJL, 953, L28
Myserlis, I., Agudo, I., Thum, C., et al. 2025, in Highlights of Spanish Astrophysics XII, Proc. of the XVI Scientific Meeting of the Spanish Astronomical Society, ed. M. Manteiga et al., 121
Myserlis, I., Angelakis, E., Kraus, A., et al. 2018, A&A, 609, A68
Nagai, H., Haga, T., Giovannini, G., et al. 2014, ApJ, 785, 53
Nagai, H., Suzuki, K., Asada, K., et al. 2010, PASJ, 62, L11
Nasa High Energy Astrophysics Science Archive Research Center (Heasarc), 2014 HEAsoft: Unified Release of FTOOLS and XANADU, Astrophysics Source Code Library, ascl:1408.004
Nilsson, K., Lindfors, E., Takalo, L. O., et al. 2018, A&A, 620, A185
Nilsson, K., Pasanen, M., Takalo, L. O., et al. 2007, A&A, 475, 199
Otero-Santos, J., Piirola, V., Escudero Pedrosa, J., et al. 2024, AJ, 167, 137
Paraschos, G. F., Debbrecht, L. C., Kramer, J. A., et al. 2024a, A&A, 686, L5
Paraschos, G. F., Kim, J. Y., Krichbaum, T. P., & Zensus, J. A. 2021, A&A, 650, L18
Paraschos, G. F., Kim, J. Y., Wielgus, M., et al. 2024b, A&A, 682, L3
Paraschos, G. F., Krichbaum, T. P., Kim, J. Y., et al. 2022, A&A, 665, A1
Paraschos, G. F., & Mpisketzis, V. 2025, A&A, 696, L7
Paraschos, G. F., Mpisketzis, V., Kim, J. Y., et al. 2023, A&A, 669, A32
Peirson, A. L., Negro, M., Liodakis, I., et al. 2023, ApJL, 948, L25
Poutanen, J. 1994, ApJS, 92, 607
Rani, B., Madejski, G. M., Mushotzky, R. F., Reynolds, C., & Hodgson, J. A. 2018, ApJL, 866, L13
Reynolds, C. S., Smith, R. N., Fabian, A. C., et al. 2021, MNRAS, 507, 5613
Saade, M. L., Kaaret, P., Liodakis, I., & Ehlert, S. R. 2024, ApJ, 974, 101
Schmidt, R. W., Fabian, A. C., & Sanders, J. S. 2002, MNRAS, 337, 71
Singh, V., Shastri, P., & Risaliti, G. 2011, A&A, 532, A84
Sinitsyna, V. G., & Sinitsyna, V. Y. 2025, ApJ, 985, 39
Soffitta, P., Baldini, L., Baumgartner, W., et al. 2023, Proc. SPIE, 12678, 1267803
Suzuki, K., Nagai, H., Kino, M., et al. 2012, ApJ, 746, 140
Tagliacozzo, D., Marinucci, A., Ursini, F., et al. 2023, MNRAS, 525, 4735
Tanada, K., Kataoka, J., Arimoto, M., et al. 2018, ApJ, 860, 74
Tugliani, S., Massaro, F., Negro, M., et al. 2025, ApJL, 985, L32
Ursini, F., Marinucci, A., Matt, G., et al. 2023, MNRAS, 519, 50
Veron, P. 1978, Natur, 272, 430
Weaver, Z. R., Jorstad, S. G., Marscher, A. P., et al. 2022, ApJS, 260, 12
Weisskopf, M. C., Soffitta, P., Baldini, L., et al. 2022, JATIS, 8, 026002
Willingale, R., Starling, R. L. C., Beardmore, A. P., Tanvir, N. R., & O'Brien, P. T. 2013, MNRAS, 431, 394
Wilms, J., Allen, A., & McCray, R. 2000, ApJ, 542, 914
Zhang, H., & Böttcher, M. 2013, ApJ, 774, 18
Zhang, H., Böttcher, M., & Liodakis, I. 2024, ApJ, 967, 93